

# Examination of the critical behavior and magnetocaloric effect of the ferromagnetic Gd-Au-Si quasicrystal approximants

Takayuki Shiino <sup>1,\*</sup>, Girma Hailu Gebresenbut,<sup>2</sup> Cesar Pay Gómez,<sup>2</sup> Ulrich Häussermann,<sup>3</sup> Per Nordblad,<sup>1</sup> Andreas Rydh <sup>4</sup> and Roland Mathieu <sup>1,†</sup>

<sup>1</sup>*Department of Materials Science and Engineering, Uppsala University, Box 35, 751 03 Uppsala, Sweden*

<sup>2</sup>*Department of Chemistry, Ångström Laboratory, Uppsala University, 751 21 Uppsala, Sweden*

<sup>3</sup>*Department of Materials and Environmental Chemistry, Stockholm University, 106 91 Stockholm, Sweden*

<sup>4</sup>*Department of Physics, Stockholm University, 106 91 Stockholm, Sweden*



(Received 14 July 2022; accepted 25 October 2022; published 3 November 2022)

We investigate the critical behavior and magnetocaloric effects of the Gd-Au-Si (GAS) ferromagnetic quasicrystal approximants, Gd<sub>13.7</sub>Au<sub>72.7</sub>Si<sub>13.6</sub> [referred to as GAS(0)] and Gd<sub>15.4</sub>Au<sub>68.6</sub>Si<sub>16.0</sub> [GAS(100)]. The former is a conventional Tsai-type 1/1 approximant crystal, while the latter has a slightly different atomic decoration from the Tsai type (thus referred to as “pseudo-Tsai” type). Their critical exponents at the ferromagnetic transitions are close to those of the mean-field theory. Both GAS systems exhibit an interesting magnetic-field dependence of the specific heat, which is reflected in the behavior of their magnetocaloric effect (MCE). The MCE is characterized by an adiabatic cooling (heating) effect over a relatively broad temperature range below ~30 K, which stems from a broad feature in the specific heat.

DOI: [10.1103/PhysRevB.106.174405](https://doi.org/10.1103/PhysRevB.106.174405)

## I. INTRODUCTION

Quasicrystals (QCs) and their approximant crystals (ACs) [1] are potential playgrounds for novel physical phenomena due to their unique atomic arrangement and crystal structures. For example, the discovery of unusual quantum criticality [2,3] and a theoretical prediction of unconventional superconductivity [4] have attracted a great deal of attention. Furthermore, long-range magnetic order in QCs was recently reported [5], which provides opportunities to investigate the physics of long-range quasiperiodic magnetic order. Despite these intriguing discoveries and predictions, some fundamental physical phenomena of QC and AC systems have not yet been thoroughly investigated. Missing tasks are, e.g., studies of critical exponents and the magnetocaloric effect (MCE) of ferromagnetic ACs. As far as we know, reports about the critical behavior of ferromagnetic ACs (and QCs) are lacking, while Ref. [6], which investigates the Au-Al-RE (RE = Gd, Tb, Dy) AC system, is the only report about the MCE of AC systems we could find at present.

Here, we investigate the critical behavior and MCE of two compositionally different Gd-Au-Si (GAS) 1/1 AC systems, Gd<sub>13.7</sub>Au<sub>72.7</sub>Si<sub>13.6</sub> and Gd<sub>15.4</sub>Au<sub>68.6</sub>Si<sub>16.0</sub>, which are named

GAS(0) and GAS(100), respectively. Note that “1/1” refers to the (first) rational approximation of the golden ratio  $\tau = (1 + \sqrt{5})/2$ , which is linked to QCs [1]. The former GAS(0) is a Tsai-type [7] AC, which is the most common type of ACs. Their building units are clusters made of four concentric polyhedral shells followed by a tetrahedral unit at the cluster center [see Fig. 1(a)]. Rare-earth (RE) atoms reside on the icosahedral shells; here, RE = Gd (magnetic). The clusters are arranged periodically in ACs and aperiodically in QCs. Figure 1(b) displays the body-centered-cubic (bcc) arrangement of the RE icosahedral shells for 1/1 ACs. The latter GAS(100) is a second type of Tsai-type 1/1 AC (referred to as “pseudo-Tsai” type) in which the orientationally disordered (Au/Si)<sub>4</sub> central tetrahedron is replaced by a single RE atom [8]. Note that the number in the parentheses indicates the percentage of pseudo-Tsai clusters, i.e., GAS(0) is a conventional Tsai-type AC, while GAS(100) is a pseudo-Tsai-type AC. The bcc arrangement of the RE icosahedral shells with pseudo-Tsai cluster-center RE atoms is displayed in Fig. 1(c).

In this study, we performed detailed magnetization and heat-capacity measurements. We find that there is no significant difference between GAS(0) and GAS(100) with respect to their critical behavior. The values of their critical exponents  $\beta$  and  $\gamma$  are close to those expected from the mean-field theory ( $\beta = 0.5$ ,  $\gamma = 1$ ), yet the values of  $\delta$  are different from the mean-field value. On the other hand, we observe an interesting broad bump in specific heat divided by temperature ( $C/T$ ) below the magnetic ordering temperatures, which is more significant in GAS(100). The specific heat exhibits significant magnetic-field dependence. These behaviors result in adiabatic temperature change over a relatively wide temperature range at low temperatures.

\*neomi.taka.shin@gmail.com

†roland.mathieu@angstrom.uu.se

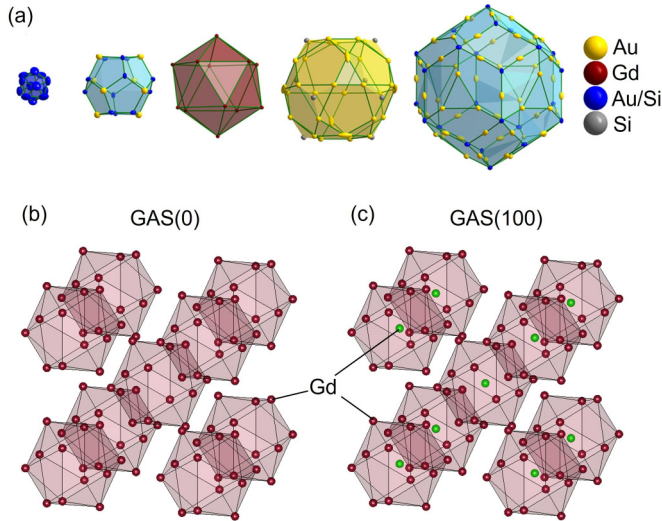


FIG. 1. (a) A Tsai-type cluster unit: From left to right, a disordered tetrahedron (plotted as a cuboctahedron), dodecahedron, RE-icosahedron (here, RE = Gd), icosidodecahedron, and rhombic-triacontahedron, respectively. The plotted polyhedra are reproduced from Ref. [8]: The refined structure model of a Gd-Au-Si standard Tsai-type 1/1 AC (space group  $Im\bar{3}$ ). Atomic positions are displayed by thermal ellipsoids at the 70% probability level. (b), (c) Schematic illustration of the body-centered periodic arrangement of RE (=Gd) atoms. (b) Tsai-type clusters: Icosahedral RE atoms (blue). (c) Pseudo-Tsai-type clusters: Icosahedral RE atoms (blue) with cluster-center RE atoms (red).

## II. EXPERIMENTAL METHODS

Samples were synthesized by a self-flux method as described in detail in Ref. [8]. We use two samples of Ref. [8], namely GAS(0) and GAS(100) [denoted GAS(IT) and GAS(CC) in Ref. [8]]. For the dc magnetization measurements, we used a magnetic property measurement system superconducting quantum interference device (MPMS XL SQUID) magnetometer and a physical property measurement system (PPMS) with a vibrating sample magnetometer option, both of which are from Quantum Design, Inc. Heat-capacity measurements were performed using a Bluefors dilution refrigerator equipped with a superconducting magnet. The heat-capacity data were collected using a differential membrane-based nanocalorimeter [9]; the conversion of the values in molar units was done by comparing the experimental data with the Debye model [10,11]. In this study, we used polycrystalline samples for the physical property measurements.

## III. RESULTS AND DISCUSSION

The GAS systems exhibit a ferromagnetic transition at  $T_c = 21.8$  K for GAS(0) and  $T_c = 16.8$  K for GAS(100) [8]. Figure 2(a) shows the temperature dependence of the magnetization  $M$  of GAS(0) for various values of magnetic fields  $\mu_0 H$ . Figure 2(b) displays the  $M$  vs  $\mu_0 H$  ( $T = 2$  K) of GAS(0). The pseudo-Tsai-type GAS(100) also exhibits similar magnetization behavior as shown in Figs. 2(c) and 2(d). Note that demagnetization effects have been taken into

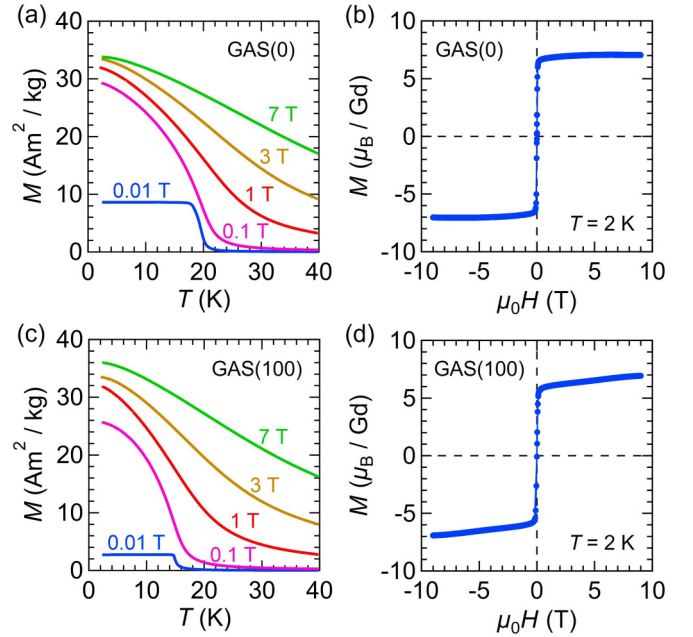


FIG. 2. (a), (b) Magnetization of GAS(0). (c), (d) Magnetization of GAS(100). (a), (c)  $M$  vs  $T$  for different magnetic fields  $\mu_0 H = 0.01, 0.1, 1, 3,$  and  $7$  T. (b), (d)  $M$  vs  $H$  at  $T = 2$  K.

account in the following analyses (see Fig. S1 in Supplemental Material [12]).

Figures 3(a) and 3(b) show  $M$  vs  $H$  curves at several temperatures in the vicinity of the transition temperatures. Figures 3(c) and 3(d) show the “modified” Arrott plots  $M^{1/\beta_A}$  vs  $(H_{\text{int}}/M)^{1/\gamma_A}$  [13], where  $(\beta_A, \gamma_A) = (0.47, 1.12)$

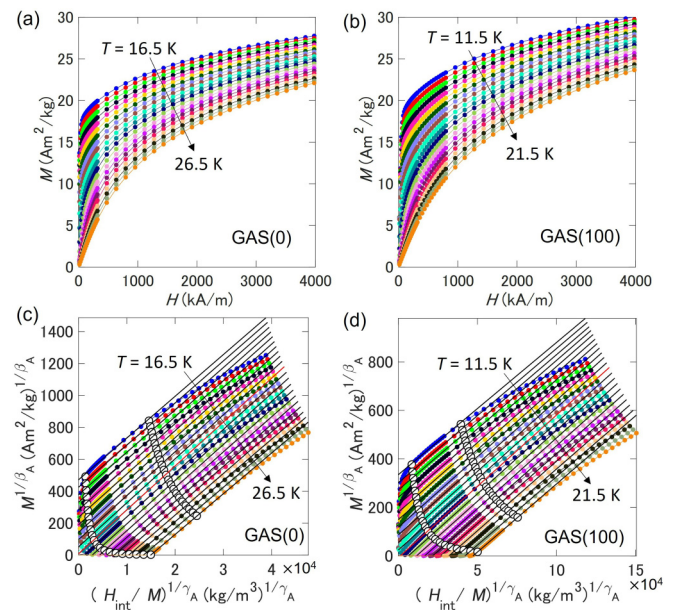


FIG. 3. (a), (b)  $M$  vs  $H$  curves at several temperatures (in 0.5 K steps) around the magnetic transition temperatures for (a) GAS(0) and (b) GAS(100). (c), (d) Arrott plot [i.e.,  $M^{1/\beta_A}$  vs  $(H_{\text{int}}/M)^{1/\gamma_A}$ ] for (c) GAS(0) and (d) GAS(100). Note that  $(\beta_A, \gamma_A) = (0.47, 1.12)$  for GAS(0) and  $(0.51, 1.01)$  for GAS(100).

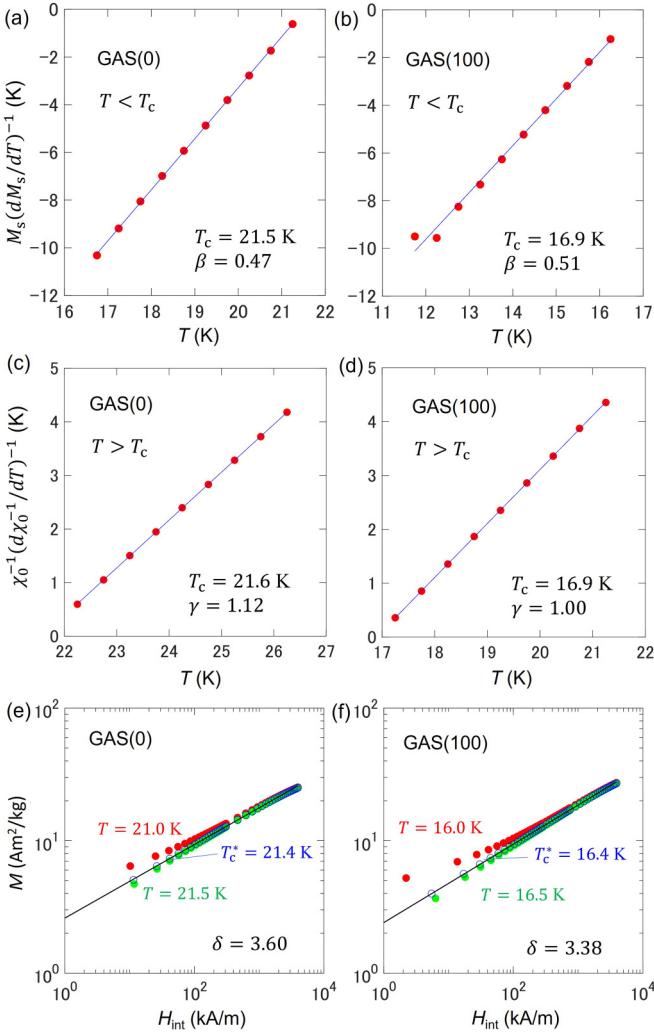


FIG. 4. (a), (b)  $M_s(dM_s/dT)^{-1}$  vs  $T$  for  $T < T_c$ . (c), (d)  $\chi_0^{-1}(d\chi_0^{-1}/dT)^{-1}$  vs  $T$  for  $T > T_c$ . (e), (f) Log-log plot of  $M$  vs  $H_{\text{int}}$  near the transition temperature.

for GAS(0) and (0.51, 1.01) for GAS(100). Note that  $H_{\text{int}}$  is the internal effective magnetic field  $H_{\text{int}} = H - NM$  where  $H$  is an external magnetic field and  $N$  is the demagnetization factor. Here, the value of  $N$  is estimated to be  $N = 0.06$  for GAS(0) and  $N = 0.18$  for GAS(100). Note that the parallel linear behavior is observed for  $0.1 \lesssim \mu_0 H \lesssim 1.5$  T [the region between the two white markers in Figs. 3(c) and 3(d)]; the line defining  $T_c$  passes through (near) the origin.

We estimate spontaneous magnetization  $M_s$  ( $T < T_c$ ) and inverse susceptibility  $\chi_0^{-1}$  ( $T > T_c$ ) from the linear extrapolation of the Arrott-plot curves [see the solid lines in Figs. 3(c) and 3(d) and Fig. S2 in Supplemental Material [12]]. Here, we employ the Kouvel-Fisher (KF) method [14] to estimate the critical exponents  $\beta$  and  $\gamma$ . According to the KF method,  $M_s(T)[dM_s(T)/dT]^{-1}$  vs  $T$  ( $T < T_c$ ) [see Figs. 4(a) and 4(b)] and  $\chi_0^{-1}(T)[d\chi_0^{-1}(T)/dT]^{-1}$  vs  $T$  ( $T > T_c$ ) [see Figs. 4(c) and 4(d)] exhibit straight lines, whose slopes give the values of  $1/\beta$  and  $1/\gamma$ , respectively. From the intercepts on the  $T$  axes, the value of  $T_c$  can also be obtained. Note that this method is based on the following equations, which are good

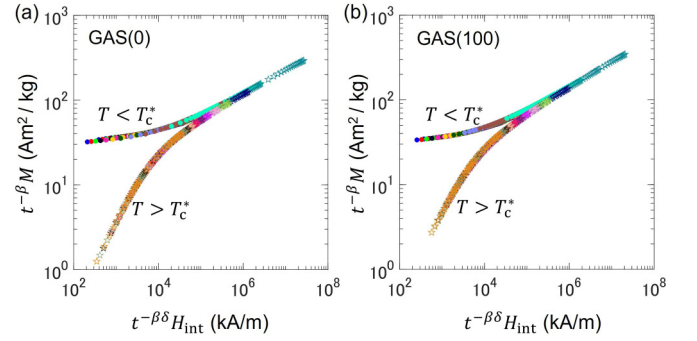


FIG. 5. Scaling plot  $t^{-\beta}M$  vs  $t^{-\beta\delta}H_{\text{int}}$  with  $t = (T - T_c^*)/T_c^*$  for (a) GAS(0) and (b) GAS(100), where  $T_c^* = 21.4$  K for GAS(0) and  $T_c^* = 16.4$  K for GAS(100). The range of the external field  $H$  is  $32 \leq H \leq 3200$  kA/m. Note that the color distinguishes the isotherms, which correspond to that of the data set in Fig. 3.

approximations near the critical region [14,15],

$$M_s(T) \left[ \frac{dM_s(T)}{dT} \right]^{-1} = \frac{T - T_c}{\beta} \quad (\text{for } T < T_c) \quad (1)$$

and

$$\chi_0^{-1}(T) \left[ \frac{d\chi_0^{-1}(T)}{dT} \right]^{-1} = \frac{T - T_c}{\gamma} \quad (\text{for } T > T_c). \quad (2)$$

The values of  $\beta$ ,  $\gamma$ , and  $T_c$  obtained from linear fitting are presented in Figs. 4(a)–4(d) and Table I. Note that the average values of  $T_c$  (from  $T < T_c$  and  $T > T_c$ ) are presented in Table I. In this analysis, we iterated the above process from the modified Arrott plot to the KF analysis by substituting  $(\beta, \gamma)$  for  $(\beta_A, \gamma_A)$  to determine the values of  $\beta$  and  $\gamma$ . From these critical values, we use Widom's identity to derive  $\delta_W = 1 + \gamma/\beta$  and Rushbrooke's identity to derive  $\alpha_R = 2 - 2\beta - \gamma$ ; the obtained values are presented in Table I.

Figures 4(e) and 4(f) show log-log plots of  $M$  vs  $H_{\text{int}}$  at two temperatures close to the estimated transition temperature  $T_c$ . The interpolated data (open symbols) at  $T_c^*$  (which is slightly different from  $T_c$  determined from the KF method) exhibit a linear behavior (see the solid line), which gives the value of  $\delta$  (see Table I). Note that  $M \sim H^{1/\delta}$  at  $T = T_c^*$ . The obtained  $\delta$  values are slightly different from those of  $\delta_W$ .

We check the scaling hypothesis  $M/|t|^\beta = f_\pm(H/|t|^{\beta+\gamma})$  where  $f_+$  and  $f_-$  are scaling functions for above and below  $T_c^*$ , respectively, and  $t = (T - T_c^*)/T_c^*$  is a normalized temperature. Figures 5(a) and 5(b) show the scaling plot of  $t^{-\beta}M$  vs  $t^{-\beta\delta}H_{\text{int}}$  with the critical exponents  $\beta$  and  $\delta$  obtained above (see Table I). We observe clear scaling behavior for  $T < T_c$  and  $T > T_c$  in both systems. Note that if we adopt  $T_c$  (determined from the KF method) instead of  $T_c^*$  for  $t$ , the scaling becomes worse for GAS(100) (see Fig. S3 in Supplemental Material [12]).

Figures 6(a) and 6(b) show the temperature dependence of the specific heat divided by temperature ( $C/T$ ) of GAS(0) and GAS(100). We observe clear anomalies at their magnetic ordering temperatures, which are significantly suppressed by the application of external magnetic fields. Interestingly, there is a broad bump below  $T_c$ , which is more significant in GAS(100) than GAS(0). Similar broad bumps appear in other Gd-based

TABLE I. Critical exponents of GAS(0) and GAS(100).  $\delta_W$  and  $\alpha_R$  are calculated from the obtained values of  $\beta$  and  $\gamma$  using Widom's identity  $\delta_W = 1 + \gamma/\beta$  and Rushbrooke's identity  $\alpha_R = 2 - 2\beta - \gamma$ . Note that the approximate errors are  $\pm 0.05$  for  $\beta$ ,  $\pm 0.1$  for  $\gamma$ ,  $\pm 0.3$  for  $\delta$ , and  $\pm 0.5$  K for  $T_c$  in the present Arrott-plot and Kouvel-Fisher analyses. Theoretical values of the exponents ( $\alpha$ ,  $\beta$ ,  $\gamma$ , and  $\delta$ ) for mean field and three-dimensional Ising, XY, and Heisenberg are also included [16].

System	$\beta$	$\gamma$	$\delta$	$T_c$ ( $T_c^*$ ) (K)	$\delta_W$	$\alpha_R$ or $\alpha$
GAS(0)	0.47	1.12	3.60	21.6 (21.4)	3.4	-0.06
$t$ or $H$ range	$-0.24 \leq t \leq -0.01$ for $T < T_c$ $0.02 \leq t \leq 0.23$ for $T > T_c$		$24 \leq H \leq 2400$ kA/m for $T = T_c^*$			
GAS(100)	0.51	1.00	3.38	16.9 (16.4)	3.0	-0.02
$t$ or $H$ range	$-0.32 \leq t \leq -0.02$ for $T < T_c$ $0.01 \leq t \leq 0.27$ for $T > T_c$		$24 \leq H \leq 2400$ kA/m for $T = T_c^*$			
Mean field	0.5	1.0	3.0			0
3D Ising	0.324	1.24	4.82			0.110
3D XY	0.346	1.32	4.81			-0.007
3D Heisenberg	0.362	1.39	4.82			-0.115

ACs [17] and QCs [5]. We calculate the magnetic entropy as follows. We estimate the magnetic contribution to the specific heat ( $C_M$ ) by subtracting the nonmagnetic (phonon and electronic) contributions. We use the nonmagnetic compounds Y-Au-Si (YAS) 1/1 ACs, i.e., YAS(0) and YAS(100) [10] (which are isostructural to the GAS systems) to estimate the

nonmagnetic part ( $C_{NM}$ ) of the GAS compounds [see the insets of Figs. 6(a) and 6(b)]. Note that we estimate  $C_{NM}$  by multiplying the temperature values by a scaling factor in the  $C$  vs  $T$  curve of the YAS compounds, according to the method described by Bouvier *et al.* [18], and normalizing it (see Fig. S4 in Supplemental Material for more details [12]). In Figs. 6(c) and 6(d), we plot  $C_M/T$  vs  $T$ . We note that the broad bumps below  $T_c$  appear to be more enhanced than the anomalies at  $T_c$ : Most of the magnetic entropy stems from the broad bumps rather than the transition at  $T_c$ . From the  $C_M/T$  curve, we calculate the magnetic entropy above the base temperature of the measurement ( $T_{\text{base}} \approx 0.2$  K), i.e.,

$$S_M(T) \equiv S_M^*(T) - S_M^*(T_{\text{base}}) = \int_{T_{\text{base}}}^T \frac{C_M}{T} dT, \quad (3)$$

where  $S_M^*(T) = \int_0^T C_M/T dT$  is a magnetic entropy measured from absolute zero. Figures 6(e) and 6(f) display the calculated magnetic entropy  $S_M(T)$  as a function of temperature. The zero-field magnetic entropy  $S_M(T)$  saturates near  $R \ln 8$  (where  $R$  is the gas constant) above  $T_c$ , in agreement with the  $\text{Gd}^{3+}$  magnetism: Note that a free  $\text{Gd}^{3+}$  ion has the total angular momentum of  $J = S = 7/2$  and thus it is  $8 (= 2J + 1)$ -fold degenerate. In the case of GAS(100), approximately half of the magnetic entropy is from the bump anomaly: Nearly half of full magnetic entropy is gained at  $T = T_c/2$  (which is above the onset of the bump anomaly). It is also found that magnetic fields suppress the magnetic anomalies at and below  $T_c$ ;  $S_M$  (for 12 T) at  $T = 40$  K is equivalent to the 64% of the full saturation magnetic entropy.

From the specific heat data, we calculate the total entropy above the base temperature of the measurement ( $T_{\text{base}}$ ) using the following equation,

$$S(T) \equiv S^*(T) - S^*(T_{\text{base}}) = \int_{T_{\text{base}}}^T \frac{C}{T} dT, \quad (4)$$

where  $S^*(T) = \int_0^T C/T dT$  is an entropy measured from absolute zero. Figures 7(a) and 7(b) show the temperature dependence of the total entropy ( $S$ ) of GAS(0) and GAS(100) for various values of external magnetic fields. We calculate the magnetic entropy change [19] from  $S$  [Figs. 7(a) and 7(b)]

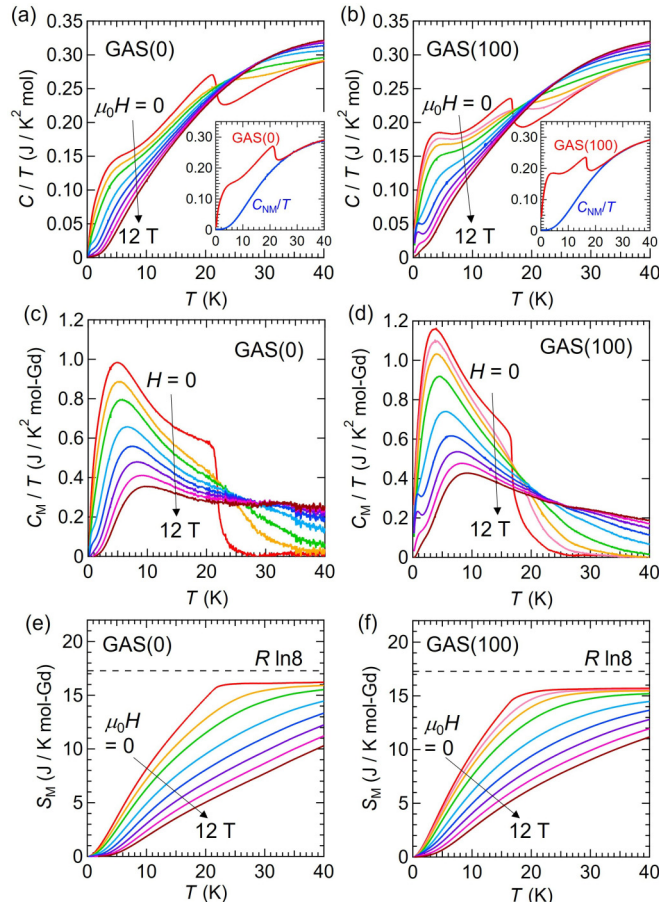


FIG. 6. (a), (b) Temperature dependence of  $C/T$  under different magnetic fields  $\mu_0 H = 0, 0.5$  [only for GAS(100)], 1, 2, 4, 6, 8, 10, and 12 T. (c), (d) Temperature dependence of  $C_M/T$ . (e), (f) Temperature dependence of  $S_M$ .

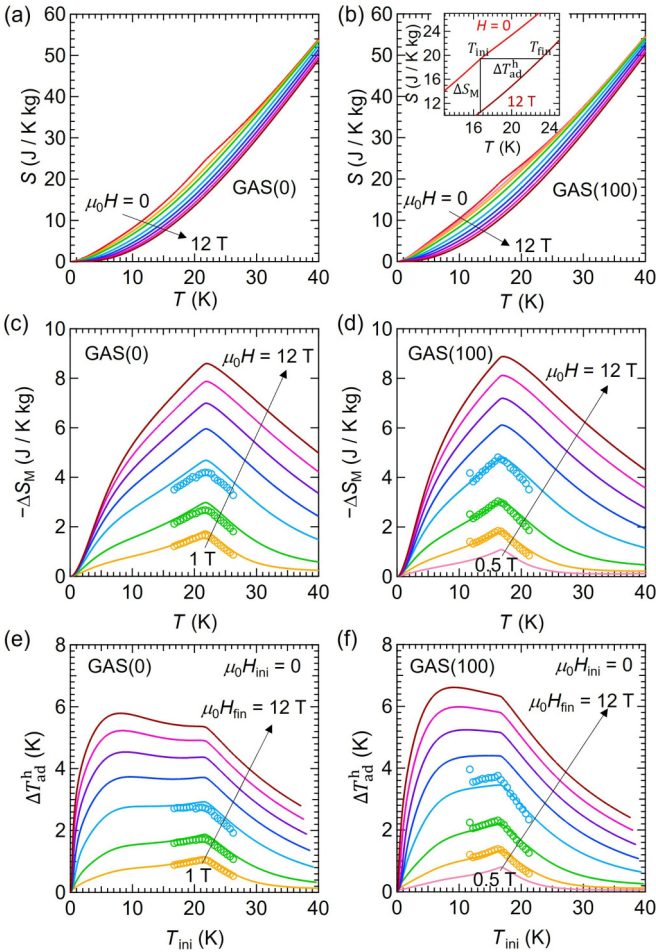


FIG. 7. Adiabatic magnetization heating. (a), (b) Temperature dependence of the total entropy under different magnetic fields estimated from the heat-capacity data. The inset in (b) explains the magnetic entropy change  $-\Delta S_M$  and adiabatic temperature change  $\Delta T_{\text{ad}}^h$  by magnetization heating. (c), (d) Temperature dependence of the magnetic entropy change  $-\Delta S_M$ . (e), (f) Adiabatic temperature change  $\Delta T_{\text{ad}}^h$  against the initial temperature  $T_{\text{ini}}$ . Data estimated considering the  $-\Delta S_M$  extracted from magnetic measurements are added using solid open markers (see main text).

or  $S_M$  [Figs. 6(c) and 6(d)] as follows:

$$\Delta S_M(T, H) = S(T, H) - S(T, 0) = S_M(T, H) - S_M(T, 0). \quad (5)$$

Figures 7(c) and 7(d) show the temperature dependence of  $-\Delta S_M$  for different  $H$  values (solid lines). The open symbols are the magnetic entropy change (for isothermal magnetization) estimated from the magnetization data (near the transition temperatures) using the following equation:

$$\Delta S'_M(T, H) = \int_0^H \frac{\partial M}{\partial T} dH. \quad (6)$$

The magnetic entropy changes estimated from the specific heat ( $-\Delta S_M$ ) and that from the magnetization ( $-\Delta S'_M$ ) are consistent. The magnetic-field dependence of  $-\Delta S_M^{\text{max}}$  (where  $-\Delta S_M^{\text{max}}$  is the maximum value of  $-\Delta S_M$  at the transition) for both GAS(0) and GAS(100) exhibits the following power-law

dependence,

$$-\Delta S_M^{\text{max}} \propto H^n, \quad (7)$$

with  $n \approx 0.6$  (see Fig. S5 in Supplemental Material [12]). The exponent  $n \approx 0.6$  is close to  $n = 2/3$  expected for systems with well-localized moments [20], which is reasonable for the present Gd-based systems.

From the total entropy data ( $S$ ) [Figs. 7(a) and 7(b)], we estimate the adiabatic temperature change (increase) by the application of an external magnetic field  $H_{\text{fin}}$  from the initial zero-field state  $H_{\text{ini}} = 0$ ,

$$\Delta T_{\text{ad}}^h = T_{\text{fin}}(H_{\text{fin}}) - T_{\text{ini}}(H_{\text{ini}} = 0), \quad (8)$$

where  $T_{\text{ini}}$  and  $T_{\text{fin}}$  are the initial ( $H_{\text{ini}} = 0$ ) and final ( $H_{\text{fin}} \neq 0$ ) temperatures, respectively [see the inset of Fig. 7(b)]. In Figs. 7(e) and 7(f), we plot the obtained  $\Delta T_{\text{ad}}^h$  as a function of the initial temperature  $T_{\text{ini}}$  for different  $H_{\text{fin}}$  values. We confirm that the following approximate equation explains the  $\Delta T_{\text{ad}}^h$  behavior (obtained from the specific heat) well near the transition temperature,

$$\Delta T_{\text{ad}}^h \approx -\frac{T}{C} \Delta S'_M, \quad (9)$$

where  $C$  is a specific heat for  $H = 0$ . Note that Eq. (9) is a good approximation near a transition where  $T/C$  varies much slower with  $H$  than  $(\partial M/\partial T)_H$  [21]: See the open symbols in Figs. 7(e) and 7(f) for  $\Delta T_{\text{ad}}^h$ . Equation (9) also works for  $C(H = 0)$  and  $\Delta S_M$  data obtained solely from specific heat near the magnetic transition by replacing  $\Delta S'_M$  with  $\Delta S_M$  in Eq. (9): See Fig. S6 in Supplemental Material [12]. We observe large discrepancies between  $\Delta T_{\text{ad}}^h$  and  $\Delta T_{\text{ad}}^h$  for large  $H$  values near the low-temperature broad bump. Such a discrepancy between the direct (here  $\Delta T_{\text{ad}}^h$ ) and indirect ( $\Delta T_{\text{ad}}^h$ ) methods can be observed at transitions where the heat capacity changes significantly with both  $T$  and  $H$  [19]. On the other hand, the quantity of  $-H(dM/dT)$ , which may be used as a simple estimate of  $-\Delta S_M$  [22], exhibits a significant deviation near the transition temperature (near the peak of  $-\Delta S_M$ ), yet its overall temperature dependence is roughly similar to that of  $-\Delta S_M$  (see Fig. S7 in Supplemental Material [12]).

Considering the temperature range investigated here, we are interested in the adiabatic demagnetization cooling effect. From the total entropy ( $S$ ) [Figs. 7(a) and 7(b)], we estimate the adiabatic temperature change (decrease) by the switch off of an external magnetic field  $H_{\text{fin}} = 0$  from the initial state  $H_{\text{ini}} \neq 0$ :

$$\Delta T_{\text{ad}}^c = T_{\text{fin}}(H_{\text{fin}} = 0) - T_{\text{ini}}(H_{\text{ini}}). \quad (10)$$

In Figs. 8(a) and 8(b), we plot the final temperature after adiabatic cooling ( $T_{\text{fin}}$ ) as a function of the initial temperature ( $T_{\text{ini}}$ ). See the inset of Fig. 8(a) for  $T_{\text{ini}}$  and  $T_{\text{fin}}$  for adiabatic cooling. Figures 8(c) and 8(d) display the adiabatic temperature change  $-\Delta T_{\text{ad}}^c$  as a function of  $T_{\text{ini}}$ .

Most cryostats based on  $^4\text{He}$  can cool samples as low as just below 2 K. Adiabatic cooling is one of the methods to cool the systems further. The cooling performance of the present systems is not as large as the top performing Gd-based metals [23], and other materials used for adiabatic demagnetization [24–26], however, we have estimated their magnetocaloric efficiency. We estimate the adiabatic temperature change by

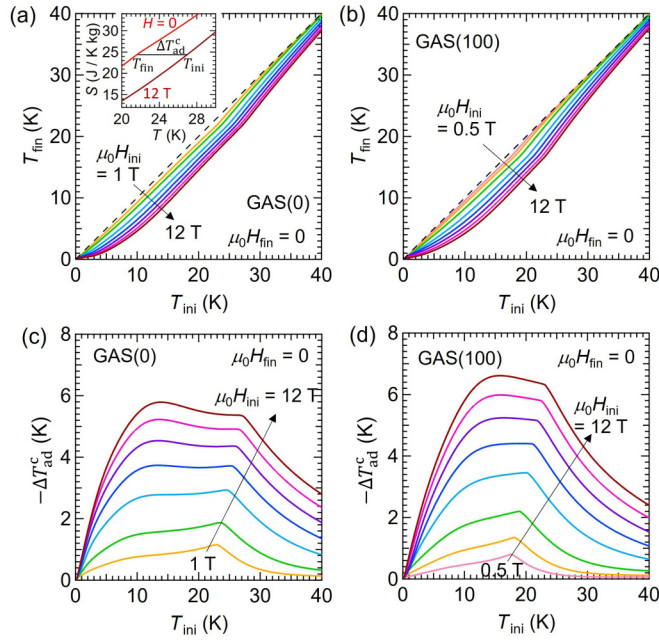


FIG. 8. Adiabatic demagnetization cooling. (a), (b) Final temperature  $T_{\text{fin}}$  vs initial temperature  $T_{\text{ini}}$ . The inset in (a) explains the adiabatic temperature change  $\Delta T_{\text{ad}}^{\text{c}}$  by demagnetization cooling. (c), (d) Adiabatic temperature change  $-\Delta T_{\text{ad}}^{\text{c}}$  against the initial temperature  $T_{\text{ini}}$ .

demagnetization cooling ( $-\Delta T_{\text{ad}}^{\text{c}}$ ) at  $T_{\text{ini}} = 2$  K. Figure 9 shows  $-\Delta T_{\text{ad}}^{\text{c}}$  vs  $\mu_0 H_{\text{ini}}$  (at  $T_{\text{ini}} = 2$  K). In the case of GAS(0), for example,  $-\Delta T_{\text{ad}}^{\text{c}} \approx 1.2$  K ( $T_{\text{fin}} \approx 0.8$  K) for  $\mu_0 H_{\text{ini}} = 6$  T, and  $-\Delta T_{\text{ad}}^{\text{c}} \approx 1.6$  K ( $T_{\text{fin}} \approx 0.4$  K) for  $\mu_0 H_{\text{ini}} = 12$  T. This indicates that by the demagnetization cooling (12 T  $\rightarrow$  0), the system temperature can be decreased by the 80% of the initial temperature (2 K). In the case of GAS(100), the value of

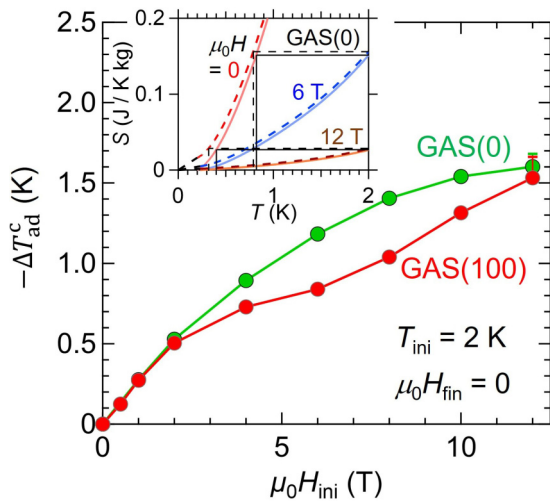


FIG. 9. Adiabatic temperature change  $-\Delta T_{\text{ad}}^{\text{c}}$  by demagnetization cooling onset at  $T_{\text{ini}} = 2$  K as a function of the initial field  $\mu_0 H_{\text{ini}}$ . The inset displays the low-temperature ( $T \leq 2$  K) part of the  $S$  vs  $T$  curves of GAS(0) [see Fig. 7(a)] for  $\mu_0 H = 0, 6,$  and  $12$  T. The dashed curves indicate those for estimated  $S^*$  with linear extrapolation below  $T_{\text{base}} \approx 0.2$  K.

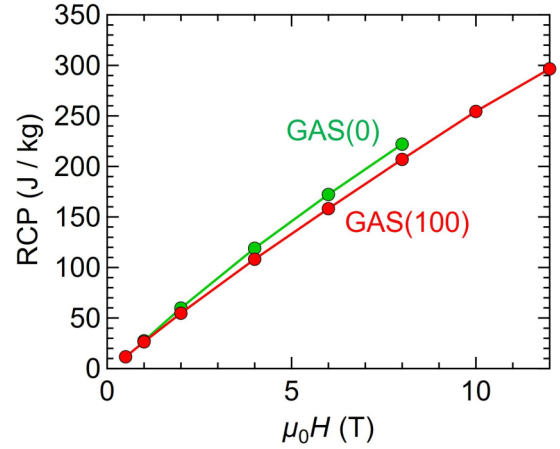


FIG. 10. RCP as a function of an applied magnetic field.

$-\Delta T_{\text{ad}}^{\text{c}}$  becomes lower than that of GAS(0) for  $2 \lesssim \mu_0 H_{\text{ini}} \lesssim 12$  T, yet it becomes comparable to GAS(0) again at 12 T. We note that the value of  $-\Delta T_{\text{ad}}^{\text{c}}$  estimated here is underestimated [21] due to the lack of specific heat data below  $T_{\text{base}} \approx 0.2$  K. We roughly estimate possible deviations from actual values as follows. First, we estimate the value of the offset  $S_{\text{base}}^*$  by linearly extrapolating the  $S$  vs  $T$  curve toward  $T = 0$  (the absolute value of the intercept at  $T = 0$  becomes  $S_{\text{base}}^*$ ). By adding  $S_{\text{base}}^*$  to  $S$ , we obtain estimated  $S^*$  vs  $T$  curves (see the dashed curves in the inset of Fig. 9). Then, we obtain the values of  $-\Delta T_{\text{ad}}^{\text{c}}$  based on the  $S^*$  vs  $T$  curves and check their deviation from those calculated based on the  $S$  vs  $T$  curves. The deviation becomes significant as  $\mu_0 H_{\text{ini}}$  becomes greater. The largest deviation (estimated here for  $\mu_0 H_{\text{ini}} = 12$  T) is  $\sim 0.08$  K for GAS(0) and  $\sim 0.13$  K for GAS(100) (indicated by the error bars at  $\mu_0 H_{\text{ini}} = 12$  T in Fig. 9). Note that the deviation estimated at  $\mu_0 H_{\text{ini}} = 6$  T is  $\sim 0.03$  K for GAS(0) and  $\sim 0.02$  K for GAS(100); the corresponding error bar is smaller than the symbol size.

In order to compare the present system with other MCE systems quantitatively, we calculate the relative cooling power (RCP) using the following equation,

$$\text{RCP} = -\Delta S_{\text{M}}^{\text{max}} \times \delta T_{\text{FWHM}}, \quad (11)$$

where  $\delta T_{\text{FWHM}}$  is the full width at half maximum of the  $-\Delta S_{\text{M}}$  curve. Figure 10 shows the RCP values as a function of an applied magnetic field  $\mu_0 H$ . Note that we could not obtain  $\delta T_{\text{FWHM}}$  (thus the RCP value) for  $\mu_0 H = 10$  and  $12$  T in GAS(0) due to the lack of data above 40 K. The value of  $-\Delta S_{\text{max}}$  amounts to about 8 J/K kg at  $\mu_0 H = 10$  T [see Figs. 7(c) and 7(d)], which means approximately 10 J/K mol Gd [ $\sim 0.6R \log(2J + 1)$ ] for GAS(0) and 8.5 J/K mol Gd [ $\sim 0.5R \log(2J + 1)$ ] for GAS(100). The RCP values at  $\mu_0 H = 5$  T (estimated by linear interpolation) are 145 J/kg (178 J/mol Gd) for GAS(0) and 132 J/kg (140 J/mol Gd) for GAS(100). These values are slightly larger than those of another MCE AC system, Au-Al-RE (RE = Gd, Tb, Dy) [6].

Other members of the RE-Au-Si family with RE = Tb and Ho were found to display glassiness in addition to long-range magnetism [27], which may stem from magnetic frustration effects. Since there is no frequency dependence in the ac

susceptibility of GAS(0) and GAS(100) [8], it seems that there is no glassy behavior in the present Gd-based system. Thus the present GAS system is different from the other RE-Au-Si family members; this might be attributed to the specificity of Gd (compared to Tb and Ho atoms), which exhibits different behavior against, e.g., crystal electric fields owing to the half-filled nature of the  $4f$  shell. The broad bump in the specific heat below  $T_c$  may stem from the specific geometry of the present magnetic system having icosahedral/octahedral networks [11,27]. Further detailed investigations are needed to clarify its origin.

#### IV. CONCLUSION

In conclusion, we have investigated the critical behavior and MCE of the GAS systems. The values of the critical exponents  $\beta$  and  $\gamma$  at the ferromagnetic transitions are close to those of the mean-field theory ( $\beta = 0.5$ ,  $\gamma = 1$ ), while the values of  $\delta$  are somewhat different from the mean-field value. The behavior of  $C_M(T)/T$  and  $S_M(T)$  presented in Figs. 6(c)–6(f)

suggests critical magnetic fluctuation in a very limited temperature range above  $T_c$ . The obtained mean-field-like values of the exponents  $\gamma$  and  $\beta$  may hence be related to the temperature ranges considered for their derivation, which may be out of the critical regime. We confirm scaling behavior with the exponents  $\beta$  and  $\delta$ . From the specific heat results, we have found that most of the magnetic entropy does not stem from the magnetic transitions at  $T_c$  but from unique broad-bump anomalies existing below  $T_c$ . These magnetic behaviors at  $T_c$  and below  $T_c$  result in moderate MCE in a relatively wide temperature range. There is no significant qualitative difference between GAS(0) (Tsai type) and GAS(100) (pseudo-Tsai type) in our results.

#### ACKNOWLEDGMENTS

We thank the Knut and Alice Wallenberg Foundation (Grant No. KAW 2018.0019) and the Carl Tryggers Stiftelse för Vetenskaplig Forskning (Grant No. CTS 19:235), and the Swedish Research Council (VR), including dnr 2021-04360.

- 
- [1] T. Fujiwara and Y. Ishii, *Quasicrystals*, Vol. 3 (Elsevier, Amsterdam, 2007).
- [2] K. Deguchi, S. Matsukawa, N. K. Sato, T. Hattori, K. Ishida, H. Takakura, and T. Ishimasa, Quantum critical state in a magnetic quasicrystal, *Nat. Mater.* **11**, 1013 (2012).
- [3] S. Matsukawa, K. Deguchi, K. Imura, T. Ishimasa, and N. K. Sato, Pressure-driven quantum criticality and  $T/H$  scaling in the icosahedral Au–Al–Yb approximant, *J. Phys. Soc. Jpn.* **85**, 063706 (2016).
- [4] S. Sakai, N. Takemori, A. Koga, and R. Arita, Superconductivity on a quasiperiodic lattice: Extended-to-localized crossover of Cooper pairs, *Phys. Rev. B* **95**, 024509 (2017).
- [5] R. Tamura, A. Ishikawa, S. Suzuki, T. Kotajima, Y. Tanaka, T. Seki, N. Shibata, T. Yamada, T. Fujii, C.-W. Wang, M. Avdeev, K. Nawa, D. Okuyama, and T. J. Sato, Experimental observation of long-range magnetic order in icosahedral quasicrystals, *J. Am. Chem. Soc.* **143**, 19938 (2021).
- [6] N. Kikugawa, T. Hiroto, A. Ishikawa, S. Suzuki, H. Sakurai, and R. Tamura, Magnetocaloric effect in ferromagnetic 1/1 quasicrystal approximants  $Au_{64}Al_{22}R_{14}$  ( $R = \text{Gd, Tb, and Dy}$ ), *J. Alloys Compd.* **882**, 160669 (2021).
- [7] A. P. Tsai, J. Q. Guo, E. Abe, H. Takakura, and T. J. Sato, A stable binary quasicrystal, *Nature (London)* **408**, 537 (2000).
- [8] G. Gebresenbut, T. Shiino, D. Eklöf, D. C. Joshi, F. Denoel, R. Mathieu, U. Häussermann, and C. Pay Gómez, Atomic-scale tuning of Tsai-type clusters in RE–Au–Si systems (RE=Gd, Tb, Ho), *Inorg. Chem.* **59**, 9152 (2020).
- [9] S. Tagliati, V. M. Krasnov, and A. Rydh, Differential membrane-based nanocalorimeter for high-resolution measurements of low-temperature specific heat, *Rev. Sci. Instrum.* **83**, 055107 (2012).
- [10] T. Shiino, G. H. Gebresenbut, F. Denoel, R. Mathieu, U. Häussermann, and A. Rydh, Superconductivity at 1 K in Y-Au-Si quasicrystal approximants, *Phys. Rev. B* **103**, 054510 (2021).
- [11] T. Shiino, F. Denoel, G. H. Gebresenbut, D. C. Joshi, Y.-C. Huang, C. P. Gómez, U. Häussermann, A. Rydh, and R. Mathieu, Singular magnetic dilution behavior in a quasicrystal approximant, *Phys. Rev. B* **104**, 224411 (2021).
- [12] See Supplemental Material at <http://link.aps.org/supplemental/10.1103/PhysRevB.106.174405> for more detailed information.
- [13] D. Kim, B. L. Zink, F. Hellman, and J. M. D. Coey, Critical behavior of  $\text{La}_{0.75}\text{Sr}_{0.25}\text{MnO}_3$ , *Phys. Rev. B* **65**, 214424 (2002).
- [14] J. S. Kouvel and M. E. Fisher, Detailed magnetic behavior of nickel near its Curie point, *Phys. Rev.* **136**, A1626 (1964).
- [15] C. Mohan, M. Seeger, H. Kronmüller, P. Murugaraj, and J. Maier, Critical behaviour near the ferromagnetic–paramagnetic phase transition in  $\text{La}_{0.8}\text{Sr}_{0.2}\text{MnO}_3$ , *J. Magn. Magn. Mater.* **183**, 348 (1998).
- [16] J. M. Coey, *Magnetism and Magnetic Materials* (Cambridge University Press, Cambridge, UK, 2010).
- [17] A. Ishikawa, T. Fujii, T. Takeuchi, T. Yamada, Y. Matsushita, and R. Tamura, Antiferromagnetic order is possible in ternary quasicrystal approximants, *Phys. Rev. B* **98**, 220403(R) (2018).
- [18] M. Bouvier, P. Lethuillier, and D. Schmitt, Specific heat in some gadolinium compounds. I. Experimental, *Phys. Rev. B* **43**, 13137 (1991).
- [19] V. K. Pecharsky and K. A. Gschneidner, Magnetocaloric effect from indirect measurements: Magnetization and heat capacity, *J. Appl. Phys.* **86**, 565 (1999).
- [20] H. Oesterreicher and F. T. Parker, Magnetic cooling near Curie temperatures above 300 K, *J. Appl. Phys.* **55**, 4334 (1984).
- [21] M. Foldeaki, W. Schnelle, E. Gmelin, P. Benard, B. Kozzegi, A. Giguere, R. Chahine, and T. K. Bose, Comparison of magnetocaloric properties from magnetic and thermal measurements, *J. Appl. Phys.* **82**, 309 (1997).
- [22] M. Hudl, R. Mathieu, P. Nordblad, S. Ivanov, G. Bazuev, and P. Lazor, Investigation of the magnetic phase transition and

- magnetocaloric properties of the  $\text{Mn}_2\text{FeSbO}_6$  ilmenite, *J. Magn. Magn. Mater.* **331**, 193 (2013).
- [23] E. C. Koskelo, C. Liu, P. Mukherjee, N. D. Kelly, and S. E. Dutton, Free-spin dominated magnetocaloric effect in dense  $\text{Gd}^{3+}$  double perovskites, *Chem. Mater.* **34**, 3440 (2022).
- [24] O. E. Vilches and J. C. Wheatley, Measurements of the Specific Heats of Three Magnetic Salts at Low Temperatures, *Phys. Rev.* **148**, 509 (1966).
- [25] D. Jang, T. Gruner, A. Steppke, K. Mitsumoto, C. Geibel, and M. Brando, Large magnetocaloric effect and adiabatic demagnetization refrigeration with  $\text{YbPt}_2\text{Sn}$ , *Nat. Commun.* **6**, 8680 (2015).
- [26] Y. Tokiwa, S. Bachus, K. Kavita, A. Jesche, A. A. Tsirlin, and P. Gegenwart, Frustrated magnet for adiabatic demagnetization cooling to milli-Kelvin temperatures, *Commun. Mater.* **2**, 42 (2021).
- [27] T. Shiino, F. Denoel, G. H. Gebresenbut, C. P. Gómez, P. Nordblad, and R. Mathieu, Nonequilibrium dynamical behavior in noncoplanar magnets with chiral spin texture, *Phys. Rev. B* **105**, L180409 (2022).